



Article

Optimization Study on Longitudinal Joints in Quasi-Rectangular Shield Tunnels

Weixi Zhang ¹, Wouter De Corte ^{1,*}, Xian Liu ² and Luc Taerwe ^{1,2}

¹ Department of Structural Engineering and Building Materials, Ghent University, 9000 Ghent, Belgium; Weixi.Zhang@UGent.be (W.Z.); Luc.Taerwe@UGent.be (L.T.)

² College of Civil Engineering, Tongji University, Shanghai 200092, China; xian.liu@tongji.edu.cn

* Correspondence: Wouter.DeCorte@UGent.be

Featured Application: (1) The damage process of the newly adopted type of longitudinal joint with ductile iron joint panels (DIJPs) in quasi-rectangular tunnels was obtained. (2) The effect of bolt position improvements was investigated through joint tests. (3) Within the service conditions, the joint behavior could be divided into three stages under both positive and negative moments. (4) Effects of the modifications related to concrete and bolt properties were explored. (5) Through comparison, increasing the lever arm between bolts and the compression zone to resist exerted moments is believed to be the most effective optimization method.

Abstract: There are large bending moments in quasi-rectangular shield tunnels due to their deviation from the circular shape, and as for other types of shield tunnels, the longitudinal joints are the most critical parts in the lining structure. A new type of joint with ductile iron joint panels (DIJPs) was installed in quasi-rectangular tunnels to solve these problems. The distance from the bolts to the segment's inner surface was improved for better performance under specific bending moment types. Both tests and finite element modeling (FEM) simulations were conducted to investigate the effect of the bolt position improvements. The resistances to crack appearance increased by 33.6% and 18.0% for positive and negative moment cases, respectively. The resistances to crack penetration increased by 13.8% and 18.4% for positive and negative cases. From the FEM approach, it was found that the behavior of the joint under the design bending moment range can be divided into three stages, whereby the bolts are only active from the second stage on. The effects of other optimizing methods, such as enhancement of concrete properties and increase of bolt diameters and numbers, are explored. Through comparison, it is believed that optimizing the joint section to increase the lever arm between bolts and the compression zone can improve the joint behavior most effectively. This optimization direction is recommended when designing a shield tunnel joint with DIJPs.

Keywords: joint behavior; joint with panels; quasi-rectangular shield tunnel; bearing capacity; numerical model



Citation: Zhang, W.; De Corte, W.; Liu, X.; Taerwe, L. Optimization Study on Longitudinal Joints in Quasi-Rectangular Shield Tunnels. *Appl. Sci.* **2021**, *11*, 573. <https://doi.org/10.3390/app11020573>

Received: 21 December 2020

Accepted: 4 January 2021

Published: 8 January 2021

Publisher's Note: MDPI stays neutral with regard to jurisdictional claims in published maps and institutional affiliations.



Copyright: © 2021 by the authors. Licensee MDPI, Basel, Switzerland. This article is an open access article distributed under the terms and conditions of the Creative Commons Attribution (CC BY) license (<https://creativecommons.org/licenses/by/4.0/>).

1. Introduction

The mechanized shield tunneling method has the advantage of a smaller environmental influence when compared with conventional tunneling methods (e.g., open cut method and blasting), and it has been widely used in urban underground space construction, from drainage tunnels to subway tunnels [1,2]. Longitudinal joints between segments divide the cross-section of a lining structure into several parts. For a certain lining shape and a given lining thickness, the joint configuration is the main factor affecting the overall lining stiffness and its deformations [3–7]. Moreover, the longitudinal joint is also the most critical part, as the lining failure is initiated by joint damage, which causes water leakage and other detrimental distress [8–11]. Therefore, the choice of the joint type is of great importance when a shield tunnel is designed.

There are two types of longitudinal joints for concrete segments connected by bolts, i.e., joints with or without preinstalled panels. In conventional circular shield tunnels, joints without panels are commonly used, as shown in Figure 1a. In order to avoid damage of the concrete near the joint, the bolt installing hole cannot be very deep in the direction to the outer segment side or very close to the joint section. This means that the possibilities of adjusting the bolt installing hole are very limited. Studies about this joint type have been conducted through experiments, simulations, and theoretical analyses [10,12–14]. In the joint type shown in Figure 1b, the joint panels are embedded into the concrete of the segments with connecting reinforcement. The panels are commonly made from ductile iron [15], and the ductile iron joint panels (DIJPs) can be cast into different shapes to achieve a more flexible bolt positioning. Joints with DIJPs have been adopted in water conveyance tunnels [16–18]. As small circumferential stresses might occur in water conveyance tunnels due to the changes of the inside water level, more bolts are needed to prevent the joints from opening [19–21]. However, fewer studies have been conducted for this joint type.

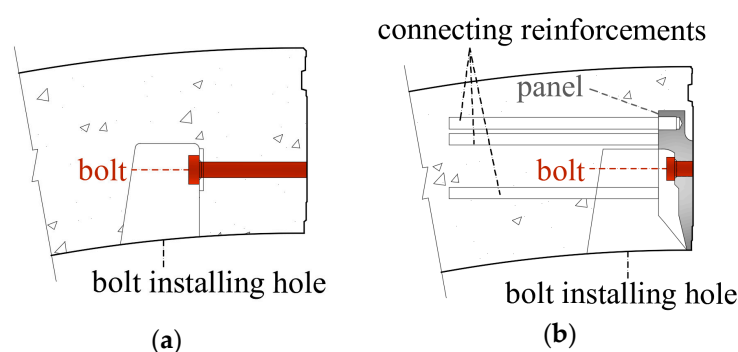


Figure 1. Two types of longitudinal joints for concrete segments connected by bolts: (a) joint without panels; (b) joint with panels.

Another important aspect is the fact that when a shield tunnel crosses a city center, the choice of the cross-section for the tunnel affects the extent of environmental influences and building or foundation settings related to tunnel construction. Quasi-rectangular shield tunnels, which have a narrow excavation width by accommodating two tracks in one tube, were introduced to reduce the environmental impact and to increase the underground space efficiency when crossing beneath a crowded urban area, as shown in Figure 2 [22,23]. Quasi-rectangular shield tunnels also have advantages such as easier control of the surface subsidence and lower cost of the segment linings when compared to other special-section shield tunnels [24–26]. However, unlike the circular lining ring, the quasi-rectangular lining shape has a reduced arching effect due to its small height-to-width ratio [27], and as a result, the bending moments in the lining are significantly larger when compared to circular linings with the same buried depth. The quasi-rectangular tunnels considered in this paper adopt joints with DIJPs to resist joint opening and rotation. As water tightness from the inner segment side is not necessary and the circumferential stresses are not reduced by the inner water pressure in quasi-rectangular tunnels, the joint section design is different from that in water conveyance tunnels. Although, as mentioned before, the joint type has an important influence on the lining's structural deformation and bearing capacity, there are few studies on the mechanical behavior of this new joint type. Moreover, behavioral insight for this joint is necessary for its further application in quasi-rectangular shield tunnels or other special-section shield tunnels with large bending moments.

In the first part of this paper, bolt position improvements of the joints with DIJPs are introduced, and joint tests before and after these improvements are conducted and compared to investigate the joint mechanical performance. The joint's ultimate bearing capacity and the failure process are explored. The components of the DIJPs and their anchorage into the concrete are proven to be reliable. Moreover, a nonlinear 3D finite element model for the local joint behavior is proposed and verified by the joint tests. In

the second part, more aspects related to the influence of the internal forces at the joint vicinity and the effects of other optimizing methods, such as enhancement of the concrete properties and increase of bolt diameters or numbers, are analyzed through the developed joint model within the bending moment range under normal service conditions.

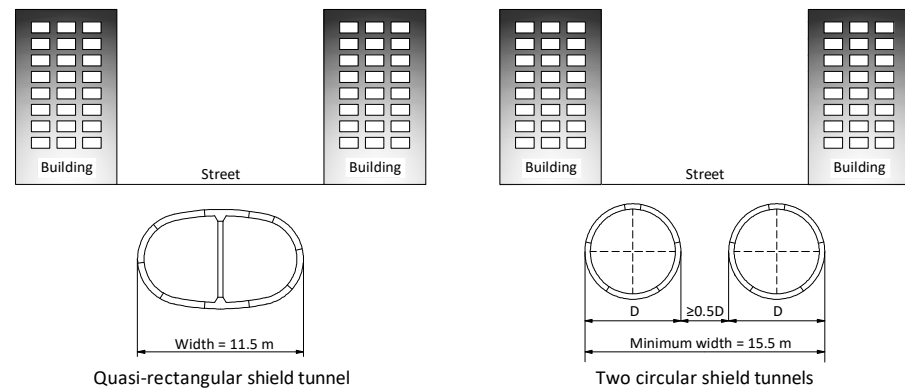


Figure 2. Comparison of a quasi-rectangular double-track shield tunnel and two circular single-track shield tunnels.

2. Test Setup

2.1. Test Specimens

Given the fact that when the joints of curved or linear lining segments sustain the same axial force and bending moment combinations, the mechanics in the joints can be considered equal [28], and the specimens in the tests were designed as planes rather than curved in order to achieve more precise bending moment values. In addition to this, all the structural details of the joints were retained as they are used in a real tunnel, such as the grooves for waterproofing belts. Each specimen was composed of two segments, and the size of each segment was $1250 \times 1200 \times 450$ mm. Two DIJPs were preinstalled in each segment through five connecting reinforcements, as shown in Figure 3. The DIJPs in adjacent segments were connected by two short straight bolts (diameter of 33 mm, yield stress of 480 MPa, tensile stress of 600 MPa). The adopted concrete class was C50 (characteristic cube compressive strength of 50 MPa). The geometric details at the joint section are shown in Figure 4.

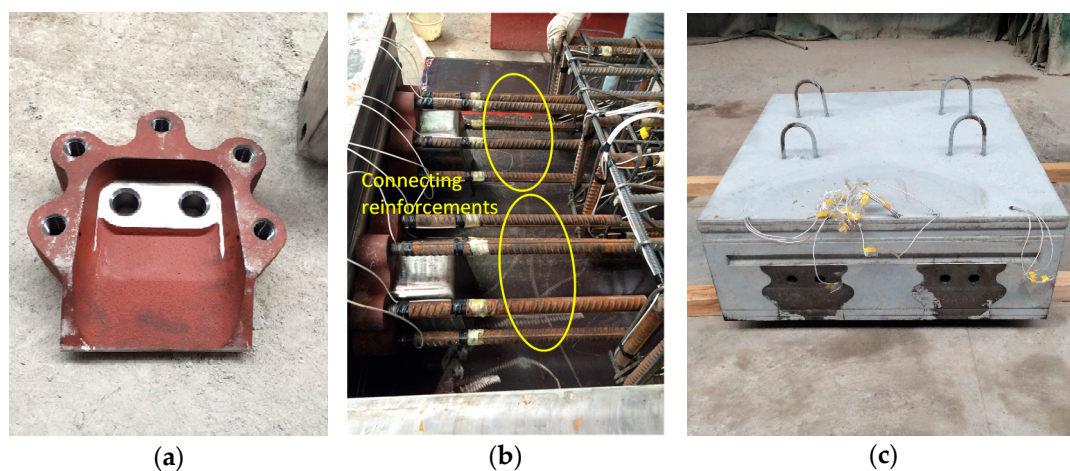


Figure 3. Tested segments: (a) ductile iron joint panel (DIJP); (b) connecting reinforcements; (c) segment after curing.

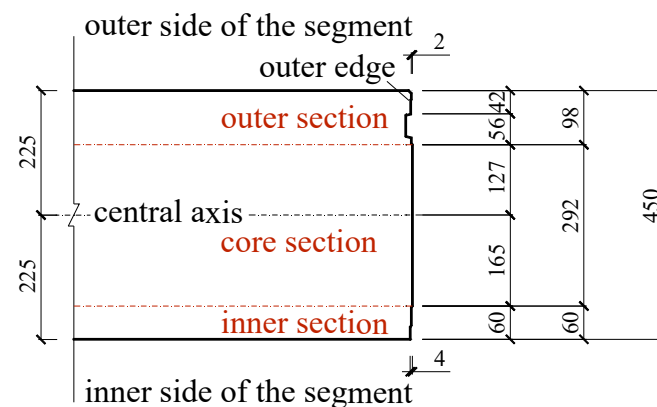


Figure 4. Geometric details of the joint section (unit: mm).

In a tunnel, the joints can be subjected to two types of bending moments, which we refer to as positive and negative bending moments. A positive bending moment creates tension at the inner side of the segment and compression at the outer side, while a negative bending moment creates the reverse stress situation. In the test specimens, the original position of the bolt was 200 mm from the inner segment surface, and we define this joint as a Type-A joint. Differently from circular tunnels, the horizontal axis of the quasi-rectangular tunnels has to be strictly controlled to be parallel to the sea level. As such, most of the longitudinal joints are subjected to either positive or negative moments only depending on their positions in the cross-section. This feature makes an optimization of the joint geometry possible based on the occurring bending moment type. It has to be pointed out that the “joint optimization” or “optimizing method” in this research does not mean that it is proven to be the best possible joint configuration; rather, it reflects a possible improved configuration compared to the original joint design. In order to increase the distance from the bolts to the compression zone so as to resist a higher bending moment, the bolts were moved 50 mm to the inner side for the joints in the case of a positive bending moment (Type-BPos joint) and 50 mm to the outer side for the joints in the case of a negative bending moment (Type-BNeg joint). The three configurations are shown in Figure 5. Each segment had two DIJPs, but only one DIJP of each segment is presented in Figure 5 for brevity. Figure 6 shows the cross-sections of the DIJPs that are indicated in Figure 5. These three configurations are used to compare the effects of the bolt position improvements.

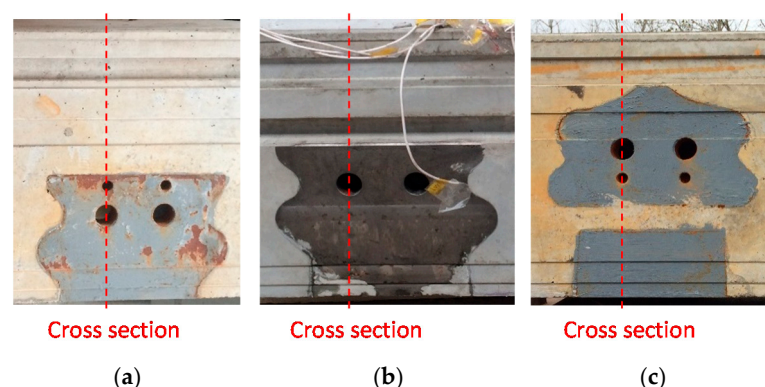


Figure 5. Front view of the DIJP configurations: (a) Type-BPos; (b) Type-A; (c) Type-BNeg.

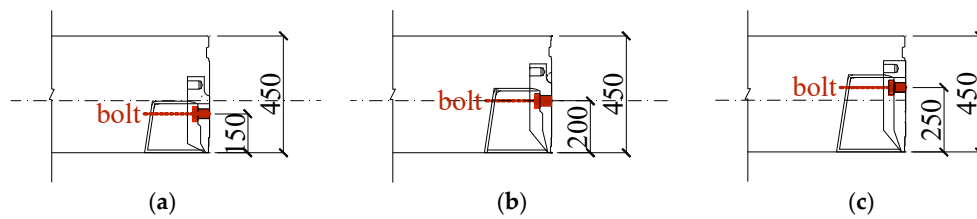


Figure 6. Cross-sectional view of the DIJPs (unit: mm): (a) Type-BPos; (b) Type-A; (c) Type-BNeg.

2.2. Testing Procedure

Positive bending moments were respectively exerted on Type-A and Type-BPos specimens, as shown in Figure 7a. The bending moment M and axial force N at the joint can be determined by the vertical loads P and horizontal loads F through

$$\begin{cases} M = P \cdot l_2 + G \cdot l_1 \\ N = F \end{cases} \quad (1)$$

and the bending moment diagram is shown in Figure 8a. Herein, P_c is the reaction force at the vertical supports, equal to the sum of the vertical load P and the dead load G . l_1 , l_2 , and l_3 represent the distances from a support to the center of gravity of each segment, to the vertical load P , and to the joint section, respectively.

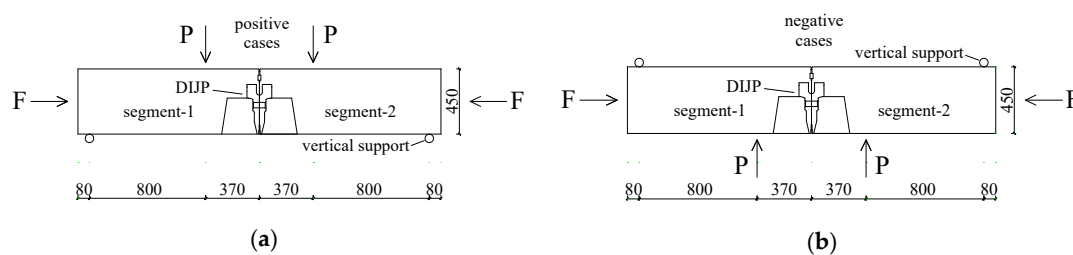


Figure 7. Exerted loads: (a) positive case; (b) negative case.

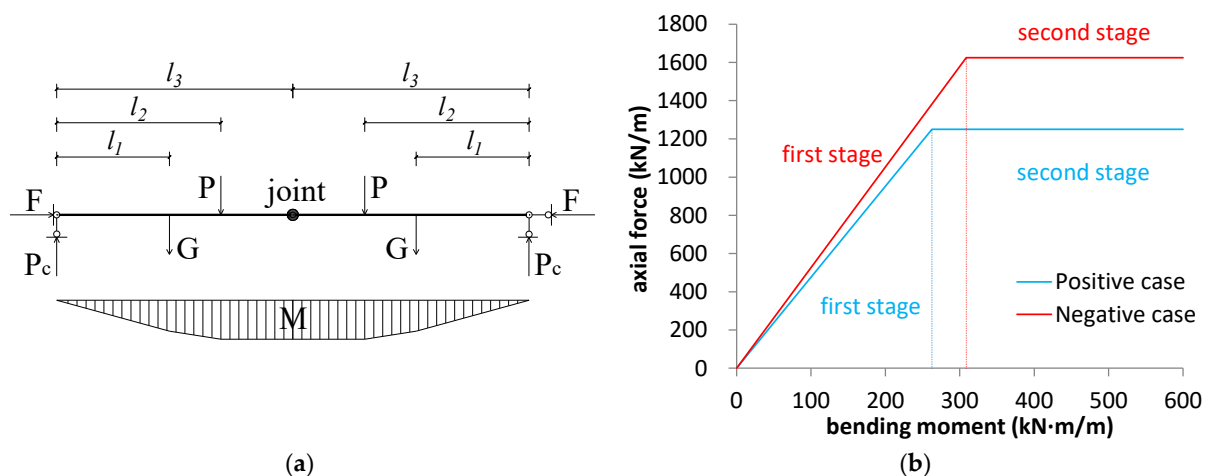


Figure 8. Test loads: (a) bending moment diagram; (b) exerted axial forces and bending moments at the joint section.

The width of the longitudinal joints in this research was 1.2 m, but this width can vary among different shield tunnels. In order to make the results independent of the segment width, the axial force and bending moment values are presented after normalization to 1 m width. As such, the units of axial force and bending moments become kN/m and kN·m/m. For the positive cases (type-A and Type-BPos), in the first testing stage, loads P and F were

increased simultaneously in order to achieve a constant eccentricity of 0.21 m up to an axial load $F = 1250 \text{ kN/m}$ ($M = 262.5 \text{ kNm/m}$). Then, in the second testing stage, only the vertical load P was increased to investigate the effect of the bending moment while the axial load F remained constant. A similar loading procedure was used for the negative cases (Type-A and Type-BNeg), as shown in Figure 8b. A constant eccentricity of 0.19 m was achieved there, up to an axial load $F = 1625 \text{ kN/m}$ ($M = 308.8 \text{ kNm/m}$), after which only the vertical load P was increased. For this case, the exerted axial forces and bending moments at the joint section are shown in Figure 8b.

During the tests, joint openings, joint deflections, bolt strains, and strains of the connecting reinforcements for the DIJPs and concrete were monitored. Strain gauges were pre-installed on the connecting reinforcements before the DIJP installation. In order to investigate the connection between the DIJPs and the concrete, the gauges were arranged to measure reinforcement strains in one transverse section, as well as along the most stressed reinforcement. The positions and numbers of the measurement points are shown in Figure 9 and Table 1.

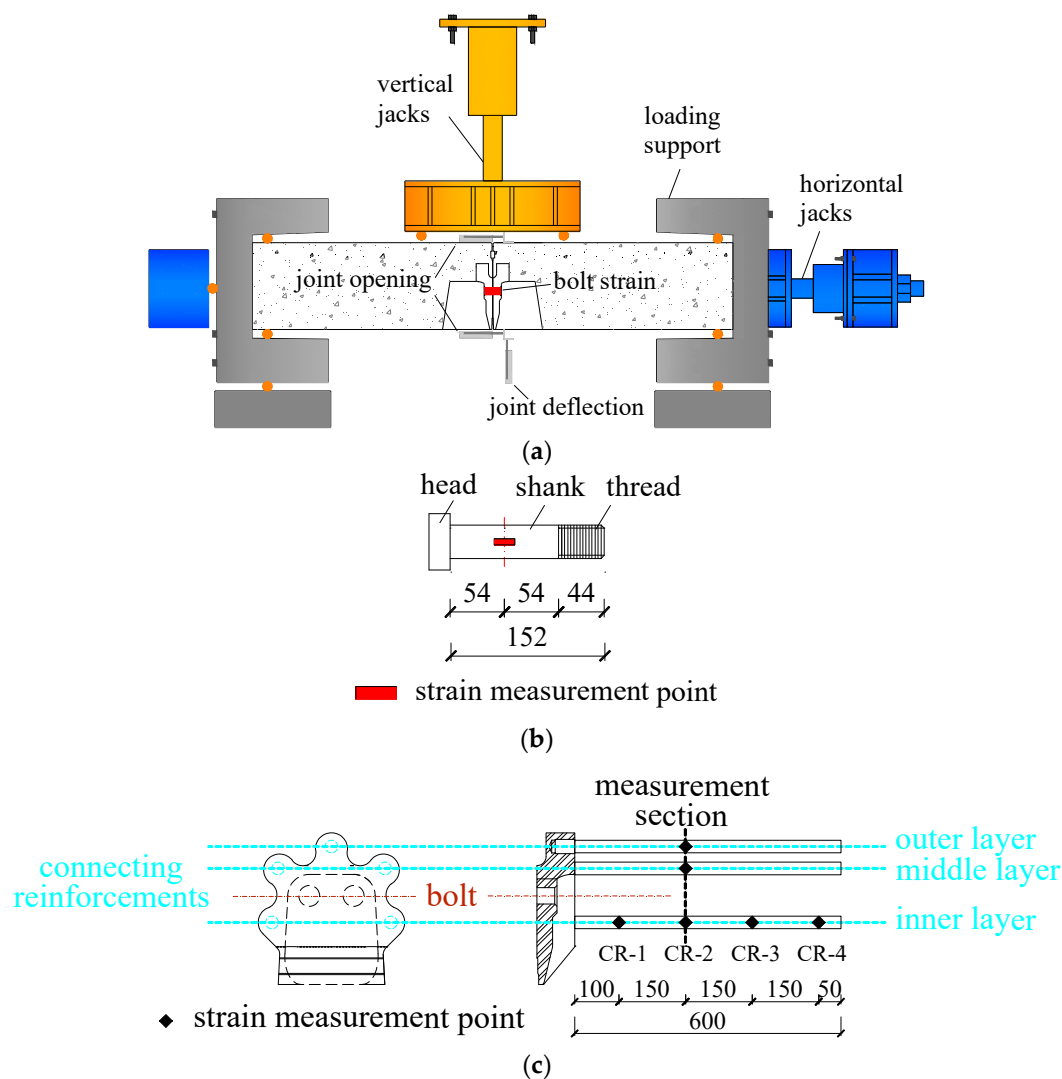


Figure 9. Measurement points: (a) joint opening, joint deflection, and bolt strains; (b) details of a bolt strain measurement point (unit: mm); (c) strain measurement points on the connecting reinforcements (unit: mm).

Table 1. List of measurement points.

Type	Quantity	Range	Accuracy
joint opening	4	0–100 mm	0.1 mm
joint deflection	2	0–100 mm	0.1 mm
bolt strain	4	0–10,000 $\mu\epsilon$	1 $\mu\epsilon$
connecting reinforcement strain	9	0–10,000 $\mu\epsilon$	1 $\mu\epsilon$

3. Numerical Model

Due to the high cost of the joint tests, only a limited number of tests could be performed. Hence, a refined nonlinear 3D joint model was developed to analyze the mechanical behavior of this new type of joint under different loading conditions and the effects of possible modifications, such as the bolt positioning, the number of bolts, or the material characteristics. For this, an Abaqus 3D joint model with all structural details was established.

Although a test specimen consisted of two segments, only one half of one segment was modelled, taking into account the symmetry of the specimen, in order to save calculation time. Hence, the joint model included one piece of DIJP, two steel washers, two halves of bolts, and half of a reinforcement cage, as shown in Figure 10. The other half of the segment was modelled through lateral symmetric boundary conditions. A rigid plate and contact conditions allowing for separation were used to represent the other segment and the other halves of the bolts. The boundary settings are shown in Figure 11.

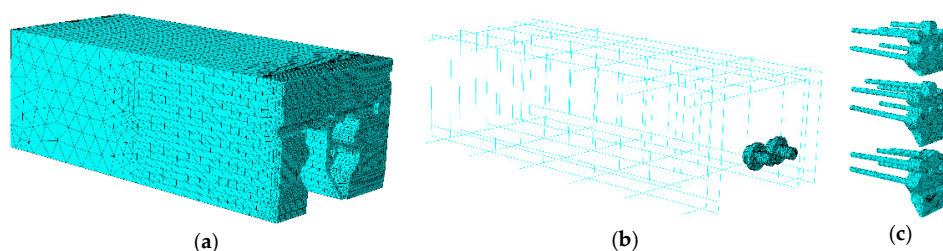


Figure 10. Joint 3D model: (a) one half of a concrete segment; (b) one half of the reinforcement cage, two halves of bolts, and two washers; (c) different DIJPs (Type-Bpos, Type-A, Type-Bneg).

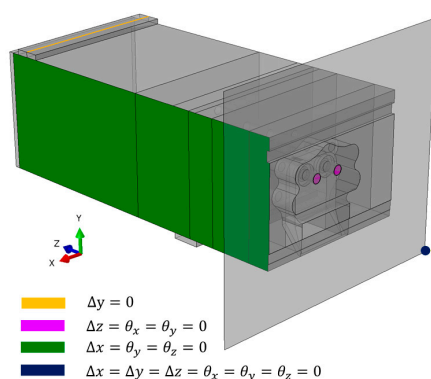


Figure 11. Model after assembly and boundary settings.

Due to the irregular contact surface between the concrete and the DIJPs in the 3D joint model, the tetrahedron element shape was adopted for meshing. The region near the joint section was finely meshed with a 10 mm element size, while the end of the joint segment was relatively coarsely meshed with a 100 mm element size. The total element number of the joint model was about 270,000. The concrete damaged plasticity model (CDP) was used for the concrete modeling, and the elastoplastic constitutive model was used for all other parts. The reinforcing cage was embedded in the concrete as a truss, and the connecting

reinforcements of the DIJP were tied to the surrounding concrete. All other contact types in the model were all set as a hard contact [29].

4. Bearing Capacity of the Joint with DIJPs

4.1. Damage Process

The effect of the bolt repositioning on the joint bearing capacity was analyzed through joint tests and finite element analysis (FEA). The obtained evolutions of the joint rotation and deflection with increasing bending moments are depicted in Figures 12 and 13. The joint rotation θ is calculated through $\theta = (v_1 - v_2)/h$, where h is the joint height of 450 mm, and v_1 and v_2 are the variations of the joint opening at the inner and outer side of the segment, which can be obtained from the joint tests or from the FEM 3D joint model.

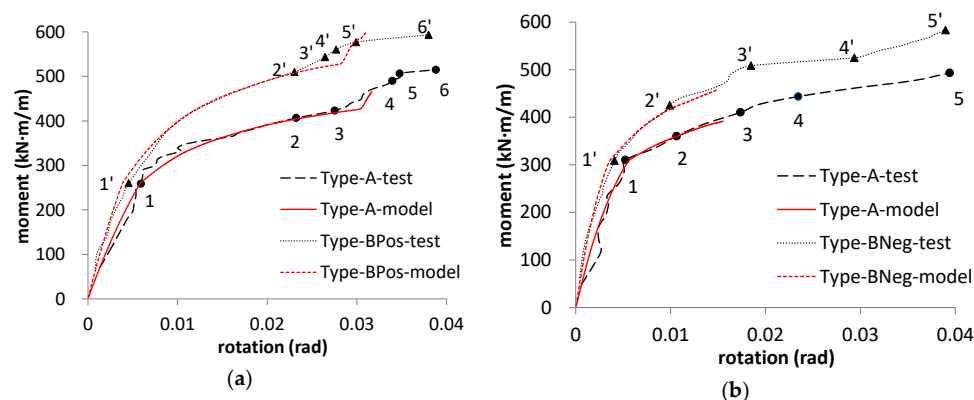


Figure 12. Evolution of the joint rotation with increasing bending moments: (a) positive cases; (b) negative cases.

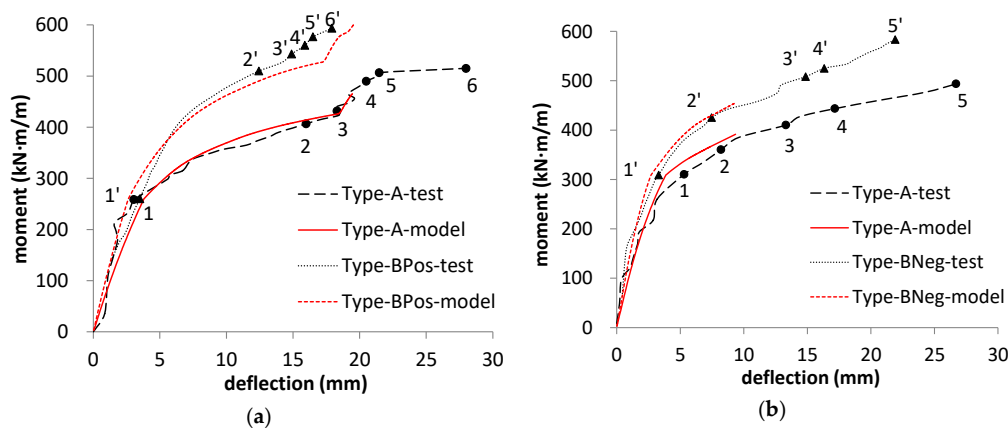


Figure 13. Evolution of the joint deflection with increasing bending moments: (a) positive cases; (b) negative cases.

Key designations (KDs) during the joint damage process (see Tables 2 and 3) are indicated with numbers 1 to 5 and 1' to 5' in Figures 12 and 13. For the positive case of the Type-A joint, after the constant axial force at the joint was attained (KD 1), the joint went through core section cracking (KD 2), outer edge contacting (KD 3), outer section cracking (KD 4), crack penetration (KD 5), and concrete crushing (KD 6). When the outer edges of the segments touched each other (KD 3), the outer part of the section started to contribute to the bending moment resistance and the speed of the joint rotation and deflection evolutions decreased. Once the crushing happened, one of the bolts snapped suddenly. Then, the tensile force in this bolt needed to be sustained by other bolts, and as a result, all bolts failed rapidly. A slightly different sequence was observed for the positive case of the Type-BPos, with the outer edges contacting each other (KD 2') before core concrete cracking (KD 3') appeared. For the negative cases, the progressive development

of the joint damage included core section cracking (KD 2 and 2'), quickly developing cracks (KD 3 and 3'), crack penetration (KD 4 and 4'), and concrete crushing (KD 5 and 5'), followed by bolt failure. The corresponding bending moments in both the positive and negative cases are summarized in Tables 2 and 3, respectively. As the damage processes before and after the improvements are similar, only pictures of the Type-A joint tests are shown in Figures 14 and 15 for brevity. The failure of the DIJP-equipped joints is initiated by core section cracking and terminated by local concrete crushing. The failure mode is similar to that of a column submitted to compound bending with small eccentricity, where the concrete is crushed before the reinforcement starts yielding.

Table 2. Key moments during the damage processes in positive cases (unit: kN·m/m).

Type-A			Type-BPos		
Key Designation	Phenomenon	Value	Key Designation	Phenomenon	Value
1	constant axial force	258.6	1'	constant axial force	260.0
2	core section cracking	406.7	2'	outer edge contacting	510.0
3	outer edge contacting	423.3	3'	core section cracking	543.3
4	outer section cracking	490.0	4'	outer section cracking	560.0
5	crack penetration	506.7	5'	crack penetration	576.7
6	concrete crushing	515.0	6'	concrete crushing	593.3

Table 3. Key moments during the damage processes in negative cases (unit: kN·m/m).

Type-A			Type-BNeg		
Key Designation	Phenomenon	Value	Key Designation	Phenomenon	Value
1	constant axial force	310.2	1'	constant axial force	308.8
2	core section cracking	360.2	2'	core section cracking	425.0
3	cracks quickly developing	410.2	3'	cracks quickly developing	508.0
4	crack penetration	443.5	4'	crack penetration	525.0
5	concrete crushing	493.5	5'	concrete crushing	583.3

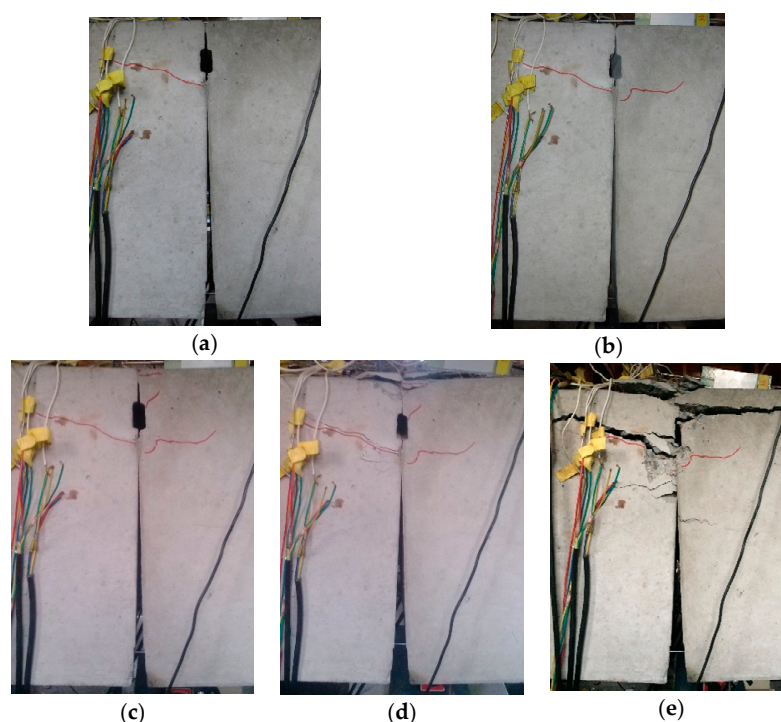


Figure 14. Type-A joint under a positive bending moment: (a) core section cracking; (b) outer edge contacting; (c) outer section cracking; (d) crack penetration; (e) concrete crushing.

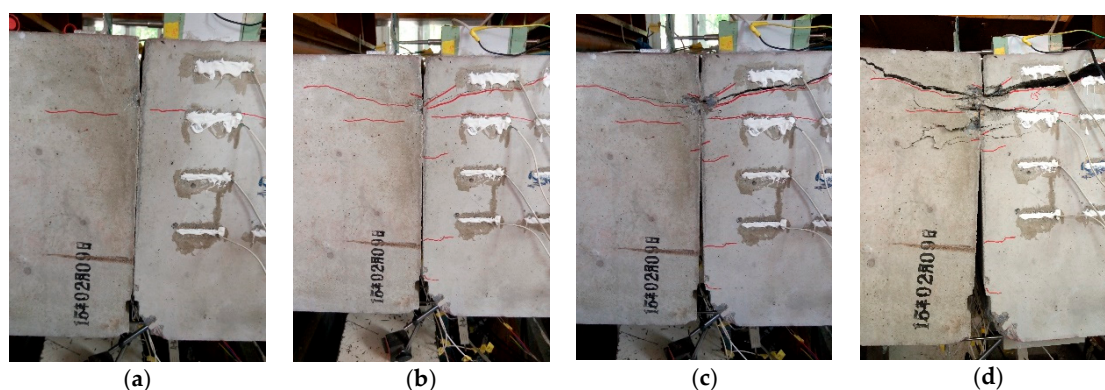


Figure 15. Type-A joint under a negative bending moment: (a) core section cracking; (b) quickly developing cracks; (c) crack penetration; (d) concrete crushing.

The noticeable core concrete cracking affects the serviceability of the segmental joint from the long-term view, as water leakage might occur or water might penetrate into the concrete and cause corrosion of the reinforcement. With this key moment chosen as a reference situation, the bolt position improvements (A to B) increase the bending moment resistance values by 33.6% for the positive cases (from 406.7 kN·m/m to 543.3 kN·m/m) and by 18.0% for the negative cases (from 360.2 kN·m/m to 425.0 kN·m/m). As soon as the cracks penetrated the segments, the compressed concrete was crushed quickly. The appearance of such penetrating cracks means that the bearing capacity of the segment is almost reached. With this key moment as a reference, the bolt improvements (A to B) increase the bending moment values by 13.8% for the positive cases (from 506.7 kN·m/m to 576.7 kN·m/m) and 18.4% for the negative cases (from 443.5 kN·m/m to 525.0 kN·m/m). It is obvious that both the joint's resistance to cracking and the ultimate bearing capacity are enhanced due to the positional improvements.

It is worth comparing the performance of a joint with DIJPs to that of the joints commonly used in conventional circular shield tunnels (see Figure 1a). From the test results for joints in a conventional circular shield tunnel [14], the bending moments when cracks appeared and cracks penetrated are compared to those from the tests for the joints with DIJPs mentioned above (see Tables 4 and 5). In addition, the corresponding rotation and deflection values are added. It should be noted that no direct comparison is possible, since the segmental thickness is not equal in both tests. Rather, the ratio between the thickness of the segments with DIJPs (450 mm) and that of the conventional joints (350 mm) is 1.29, and correspondingly, the ratio between the moments of inertia is 2.13. In the case of a comparison to the Type-A configuration, the bending moment resistances to cracking and crack penetration of the DIJP joint are more than twice those from the conventional one, which is generally consistent with the inertia moment ratio. After the bolt position improvements (Type-BPos and Type-BNeg), the resistances to cracking and crack penetration are clearly higher, and even under these large bending moments, the improved joints have smaller deflections.

Table 4. Comparison between the joints with DIJPs and joints in a conventional circular tunnel in positive cases.

Phenomenon	Bending Moment (kN·m/m)			Rotation (rad)			Deflection (mm)		
	Circular Tunnel	Type-A	Type-BPos	Circular Tunnel	Type-A	Type-BPos	Circular Tunnel	Type-A	Type-BPos
core concrete cracking	155.0	406.7	543.3	0.030	0.023	0.026	18	16.0	14.9
crack penetration	200.0	506.7	576.7	0.045	0.035	0.030	28	21.5	16.5

Table 5. Comparison between the joints with DIJPs and joints in a conventional circular tunnel in negative cases.

Phenomenon	Bending Moment (kN·m/m)			Rotation (rad)			Deflection (mm)		
	Circular Tunnel	Type-A	Type-BNeg	Circular Tunnel	Type-A	Type-BNeg	Circular Tunnel	Type-A	Type-BNeg
core concrete cracking	160.0	360.2	425.0	0.040	0.011	0.010	22	8.2	7.3
crack penetration	200.0	443.5	525.0	0.060	0.023	0.029	31	17.2	16.3

In Figures 12 and 13, the slopes of the moment–rotation curves represent the joint rotational stiffness, showing that after bolt position improvements, the rotational stiffness is also increased. These observations mean that the improvements not only contribute to a larger bearing capacity, but also to a better structural deformation control. Hence, joints adapted to the sign of the bending moment are preferable in quasi-rectangular shield tunnels, as they can sustain larger bending moments and also reduce overall lining deformations when compared to a single-joint type.

In addition, in Figures 12 and 13, the curves of joint rotations and deflections obtained from the 3D joint model are consistent with those from the tests. The bending moments in the joints of quasi-rectangular tunnels are normally within 300 kN·m under service conditions, or 250 kN·m/m after normalization [30–32]. The calculation results from the proposed joint model can cover this bending moment range well, and therefore, the developed joint model provides an effective and economical approach for studying the joint behavior within the moment range at the normal service level. The related aspects are discussed in Section 5.

4.2. Bolt Strains

In the tests, after the concrete was crushed, the compressive area moved close to the central axis of the joint section. Due to the reduced lever arm, the joint opening increased considerably, and bolts were rapidly subjected to more tension to balance the moment until they snapped one by one. Due to the stiff contact between the bolt head and the pre-installed DIJP, the bolts were not under pure tension when the joint rotated. The FEM revealed that stress concentrations appeared at the transition area between the bolt head and bolt shank, and the bolts indeed failed in this area in the tests, as shown in Figure 16.

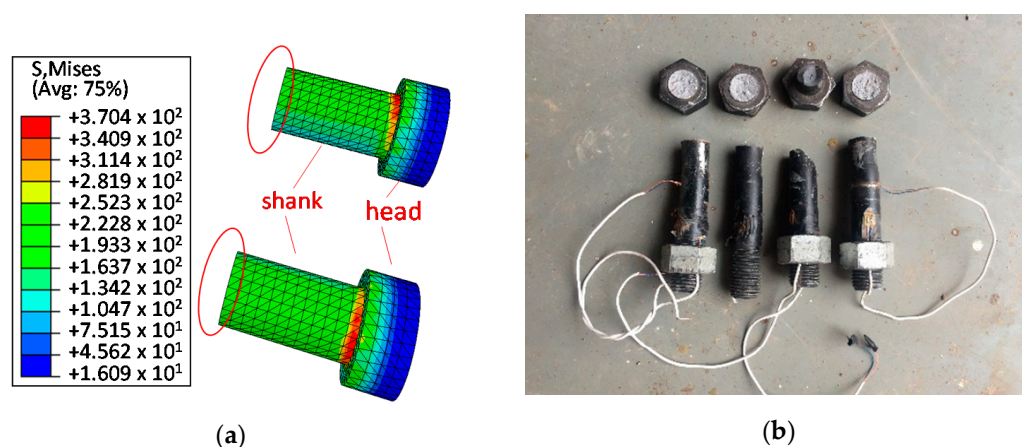


Figure 16. Bolts in the model and tests: (a) calculated bolt stress concentration in the model (33 mm diameter); (b) failed bolts in tests.

In the tests, the bolt strains were measured at the middle of the shank, as shown in Figure 9b. Correspondingly, the bolt strains in the models were also recorded at these locations, i.e., the red circles in Figure 16a. The bolt strain curves are depicted in Figure 17 for the joints with only positional improvement for brevity. In the tests, the recorded strains for different measurement points showed some variation, which was consistent with the observation that bolts broke consecutively and not simultaneously. In spite of this variation, the strain curves are similar to that from the joint model, and therefore, the bolt strains from the model can be used to predict the overall bolt strain in reality. The bolt strains prior to concrete crushing are much smaller than the yield strain of $2400 \mu\epsilon$ at $300 \text{ kN}\cdot\text{m}/\text{m}$, which means that the bolts still have a large strength margin until the concrete is crushed.

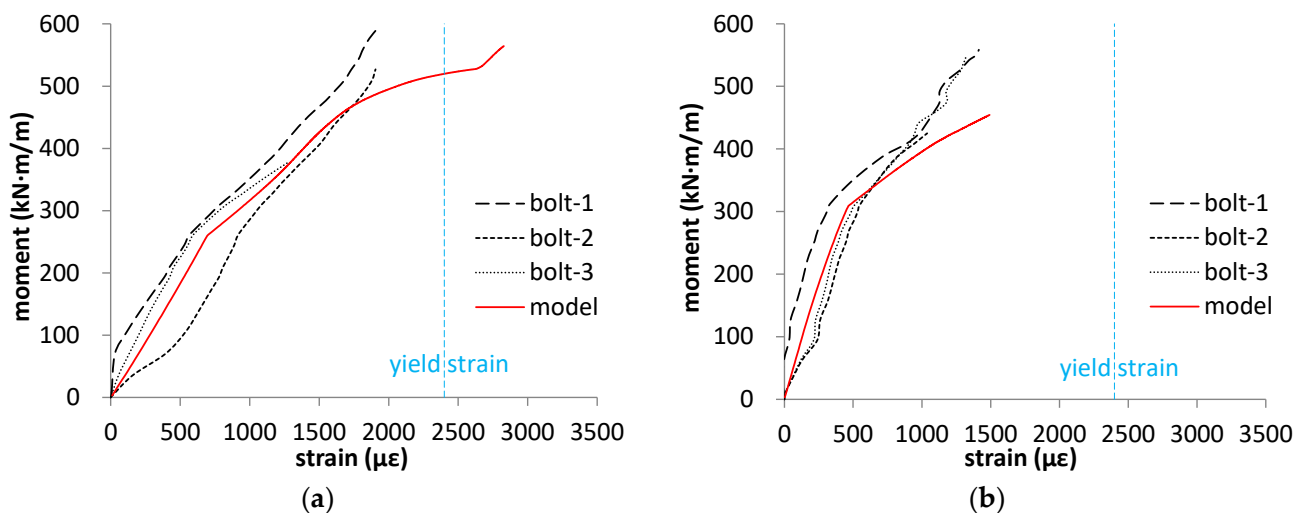


Figure 17. Evolution of the bolt strains with increasing bending moments: (a) Type-BPos joint in positive cases; (b) Type-BNeg joint in negative cases.

4.3. Connecting Reinforcement Strains

The connecting reinforcements are used to anchor the DIJPs in the concrete, and a reliable connection is important for the joint safety. As an example, the strains from the Type-A joint under positive bending moments at the measurement points indicated in Figure 9c are shown in Figure 18. In Figure 18a, the strains along the connecting reinforcement at the inner layer, which is the most stressed reinforcement in this test case, are shown. The closer to the joint section, the larger the strains are. For the strains of the connecting reinforcements at different layers, it is obvious that the inner layer resists most of the tension force, as can be seen in Figure 18b. When the bending moment is small, the middle and outer layers are under compression. As the joint is rotating, the connecting reinforcements are gradually submitted to tension forces. The trends of the strain curves obtained from the joint model and from the tests are generally in good agreement. For the bending moment equal to $300 \text{ kN}\cdot\text{m}/\text{m}$, the strains of all connecting reinforcements are smaller than $200 \mu\epsilon$. Figure 19 shows a joint section after testing. Both DIJPs are still in good condition, and few cracks have appeared around them. From this, it can be concluded that the DIJPs, as well as their connections to the concrete, have proved to be reliable.

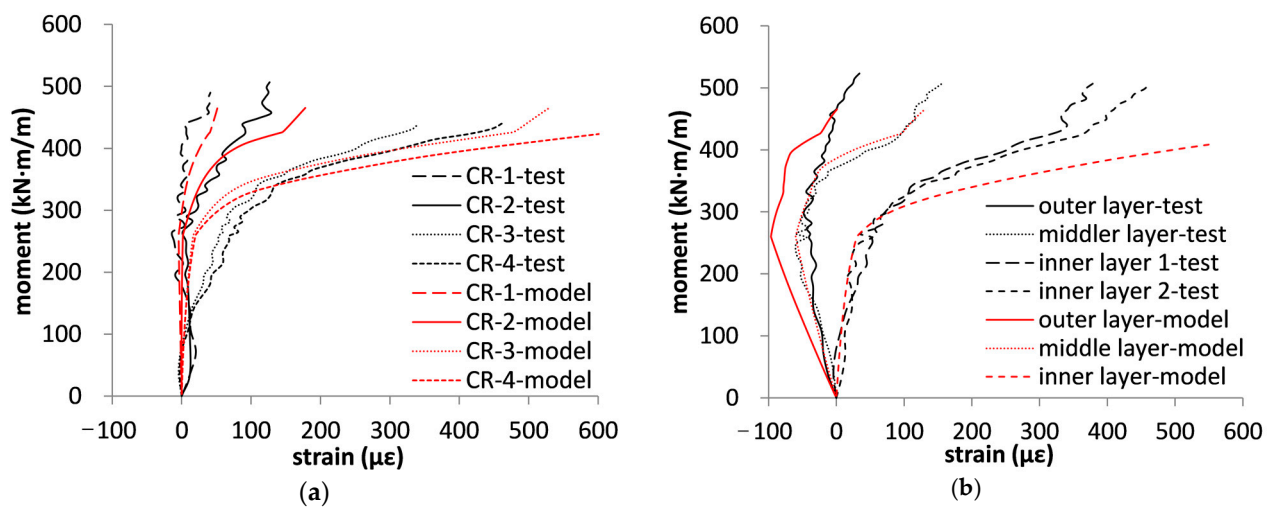


Figure 18. Evolution of the connecting reinforcement strains with increasing bending moments: (a) along the inner layer; (b) on different layers at the measurement section.

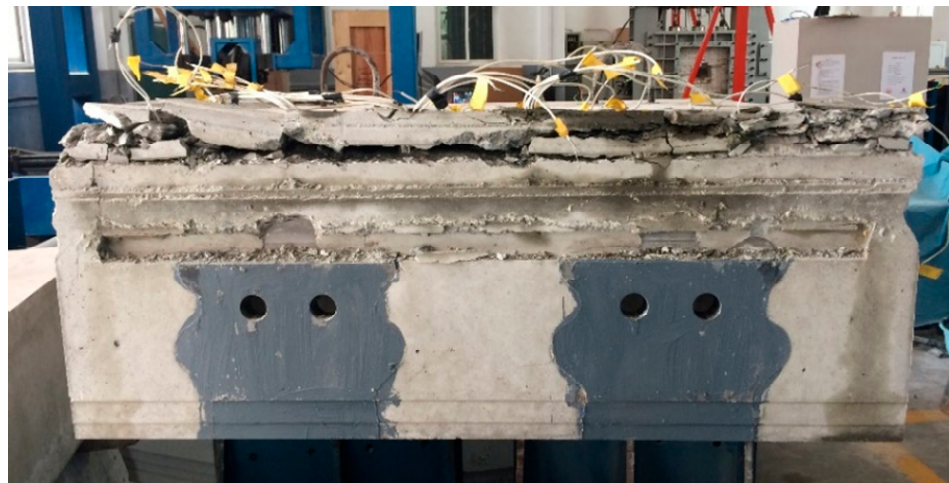


Figure 19. Joint section after testing (Type-A).

5. Parametric Study

Not only the bearing capacity of this new type of shield tunnel joint was considered, but also its rotational behavior under normal service conditions. The joint rotation results in rigid body displacements of the segments, which contribute a non-negligible part to the tunnel lining's overall deformation [11,13]. Additionally, controlling the overall deformation is an essential performance assessment index, which often governs the thickness of the lining structure. Differently from the joints in conventional circular shield tunnels, the joints in quasi-rectangular tunnels are equipped with DIJPs, and the theoretical analysis of their rotational behavior is complicated. By means of the proposed 3D joint model, more results focusing on the joint rotation within the bending moment range under normal service conditions could be obtained. As the axial forces and bending moments change together in the first stage of the joint tests, in this section, the axial force is kept constant at different levels and the bending moment increases gradually to investigate the different stages of the joint rotation development. Finally, the influences of bolt and concrete properties are investigated.

5.1. Internal Forces in the Joint's Vicinity

The axial force in the considered type of quasi-rectangular tunnel ranges from 500 to 1200 kN for a segment width under the targeted overburden from 7 m to 17 m [30–32]. Therefore, the axial force is kept constant at 400, 800, and 1200 kN in the model calculations, namely 333, 667, and 1000 kN/m after normalization.

Figure 20 presents the joint rotation curves of both original and improved bolt position joints. Figure 21 presents the bolt stress curves for the improved joints. The bolt stress curve of the original joint under 667 kN/m axial force is added to compare the effect of the improvement. Figure 22, taking the example of a positive case, shows the stress distributions at the joint section. At the first stage, when the bending moment is small, the rotation curves are similar. This means that joint rotations are not influenced by the axial forces at this stage. It is worth noting that, at this stage, the rotational stiffnesses are quite large and the bolts do not take any force. During this period, the eccentricity h_e resulting from the combined effect of the exerted moment and axial force, as shown in Figure 22, is small, and the application point of the resultant force is close to the central axis of the joint section. The whole joint core section is under compression, but its outer side is more stressed than the inner side (stress distribution-1 in Figure 22). As the bending moment keeps increasing, the eccentricity h_e increases, and the whole core section is not compressed anymore, leading to the joint opening (stress distribution-2 in Figure 22). The variation of the joint opening is mainly caused by the compressive deformations. This means that the joint behavior at this stage is determined by the height of the joint core section. At the second stage, when the neutral axis moves above the position of the bolt axis, the bolts start being tensioned and are involved in the joint rotation (stress distribution-3 in Figure 22). From Figures 20 and 21, it can be seen that the bolt stress increases quickly while the rotational stiffness decreases gradually. At the third stage, the eccentricity h_e increases further and exceeds the distance between the edge of the outer section and the joint central axis, namely $h_1 - h_c$ (stress distribution-4 in Figure 22). However, the stress distribution in the compression zone at the joint section cannot exceed this distance. From the rotation and bolt stress curves, at this stage, the rotation curve appears to be almost linear, while the bolt stress also follows a linear trend. For the same joint type under different axial forces, the stiffnesses at this stage appear to be the same.

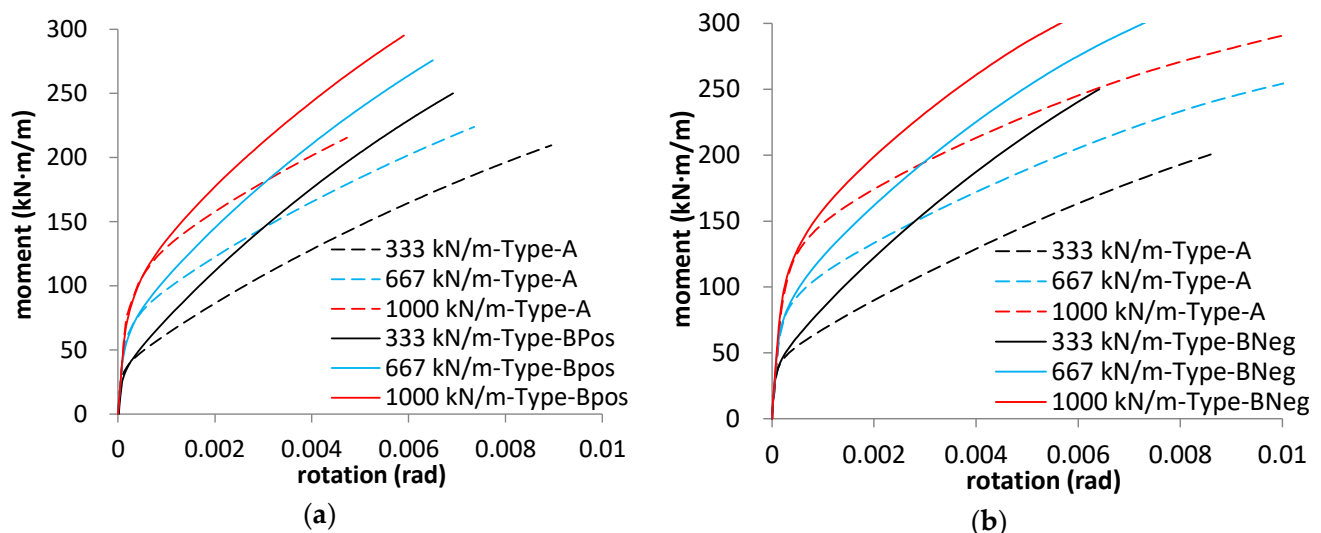


Figure 20. Evolution of the joint rotation with increasing bending moment under constant axial force: (a) positive cases; (b) negative cases.

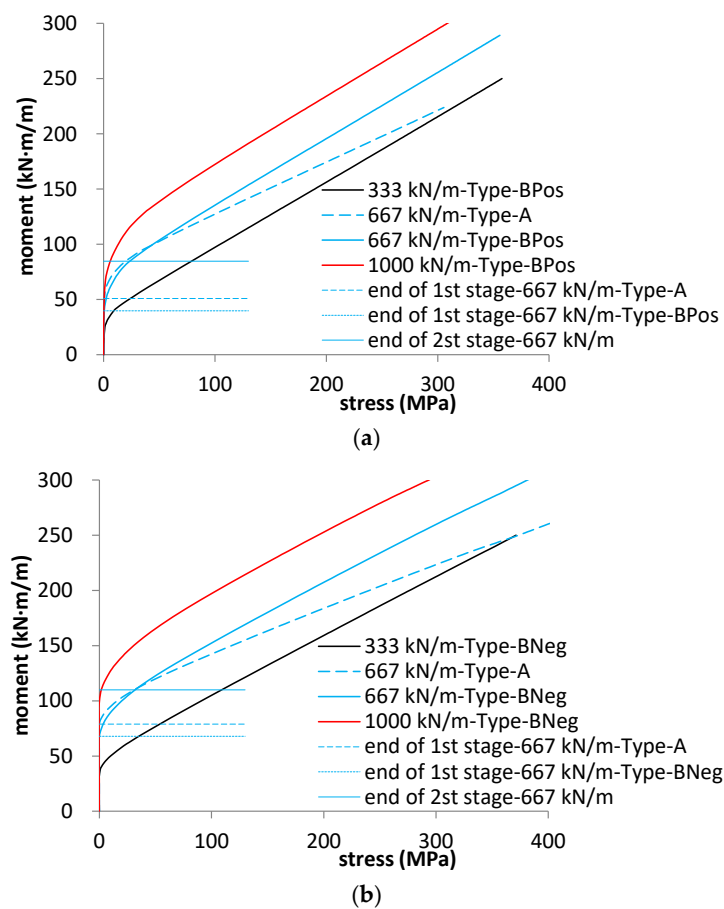


Figure 21. Evolution of the bolt stresses with increasing bending moment under constant axial force: (a) positive cases; (b) negative cases.

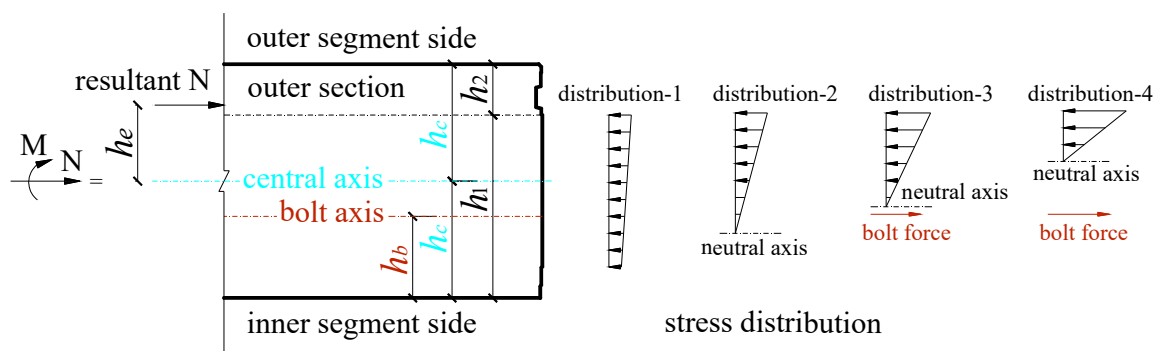


Figure 22. Stress distributions at the joint core section in a positive case.

From Figure 22, the bending moment values at the end of the first stage and the second stage can be evaluated. As the stress level at the first stage is not large, based on the assumption of a plane strain distribution, the stress distribution is assumed to have a triangular shape, and it balances the exerted axial force N and bending moment M . When the neutral axis is at the bolt axis, the first stage ends. The corresponding moment value can be calculated with Formula (2). For the end of the second stage, the eccentricity h_e equals $h_1 - h_c$, and the corresponding moment value can be calculated from Formula (3). The bending moments at the ends of these two stages are summarized in Table 6 for all calculated cases. Only the results for the 667 kN/m axial force cases are added to Figure 21 as examples to show the trend of the stress curves at different stages.

The calculated bending moments yield good predictions of the transition points between consecutive stages.

$$M_{1-2} = \left(\frac{2}{3}(h_1 - h_b) + h_b - h_c \right) \cdot N = \left(\frac{2}{3}h_1 + \frac{1}{3}h_b - h_c \right) \cdot N \quad (2)$$

$$M_{2-3} = (h_1 - h_c) \cdot N \quad (3)$$

Table 6. Summary of the bending moments at the ends of different stages.

	Axial Force (kN/m)	Positive Cases		Negative Cases	
		Type-A (kN·m/m)	Type-BPos (kN·m/m)	Type-A (kN·m/m)	Type-BNeg (kN·m/m)
End of the first stage	333	25.4	19.9	39.4	33.9
	667	50.9	39.8	78.9	67.8
	1000	76.3	59.7	118.3	101.7
End of the second stage	333		42.3		55.0
	667		84.7		110.0
	1000		127.0		165.0

When the axial force is fixed, at the first stage, the components only providing tensile force, such as bolts, do not contribute to the rotation resistance. Therefore, the joint rotational stiffness is dominated by the height of the core section. At the second stage, the tension-resistant components start working and influence the joint rotations. The bolt position improvements increase the distance from the bolts to the compression zone, providing a larger lever arm to balance the exerted moments. Consequently, the bolt stresses decrease under the same bending moment. Meanwhile, the bolt position improvements make the first stage end, and the bolts to start working slightly earlier than in the reference Type-A. It is obvious that increasing the lever arm has a significant effect on the joint stiffness values. As shown in Table 7, by calculating the slope of the curves during the third stage in Figure 20, it follows that the rotational stiffness is increased by 67% to 69% for the positive cases and by 97% to 106% for the negative cases.

Table 7. Summary of the rotational stiffnesses during the third stage under different axial forces (stiffness unit: kN·m/m/rad, axial force unit: kN/m).

Axial Force	Rotational Stiffness in Positive Cases			Rotational Stiffness in Negative Cases		
	Type-A	Type-BPos	Increase Rate	Type-A	Type-BNeg	Increase Rate
333	22,591	37,809	67%	17,030	33,490	97%
667	22,069	37,404	69%	16,076	32,598	103%
1000	21,898	37,103	69%	14,604	30,106	106%

On the other hand, it is found that, even under the same axial force, the joint stiffness deviates a lot when different bending moments are applied. Due to the higher number of joints in large-section circular shield tunnels and special-section shield tunnels than in conventional circular tunnels, these joints have different rotational stiffnesses, and the influence of the stiffness differences of these joints on the lining calculation needs to be given due attention [32].

5.2. Influence of Bolt Properties

As mentioned before, improving the bolt positions to increase the lever arm for balancing the exerted bending moment has a significant effect on the joint rotation behavior for the second and the third stages. For a fixed distance between the bolts and the core segment edges, the bolt diameter and the number of bolts can be varied to see the influence

on the joint rotational behavior. The essence of these two methods is to enhance the bolts' deformation resistance to a tensile force. The changes of the bolt diameter or the number of bolts might need shape changes of the DIJPs and redesign of the joint. In order to avoid these changes, the Young's modulus of the bolts in the model is adjusted as the only variable to simulate the effect of the enhancement of the bolts' deformation resistance. The bolt diameter of the studied joint is 33 mm and the Young's modulus is 200 GPa. The Young's modulus is reset to 372 and 661 GPa to simulate the elongation of bolts with 45 and 60 mm diameters under the same tensile force conditions. The increase of the Young's modulus could also be regarded as more bolts to resist the same tensile force. It has to be pointed out that this simplified method aims to simulate the effect of the bolt elongation resistance on joint rotations under a normal bending moment range, rather than the effects related to bolt strength or joint bearing capacity. Only the results from positive cases under the constant 667 kN/m axial force are presented in Figure 23 for brevity. The bolts' stress curves for the adjusted moduli are almost identical to that for the original modulus. Due to the modulus increase, identical stresses result in smaller bolt elongations and, consequently, in smaller joint openings. Therefore, the joint stiffness increases, as shown in Figure 23. The average rotational stiffnesses during the third stage with the Young's moduli of 372 and 661 GPa are summarized in Table 8. For the positive cases, the average stiffness at the third stage increases by 15% and 23%, respectively. Correspondingly, the stiffness increases for the negative cases are 18% and 30%.

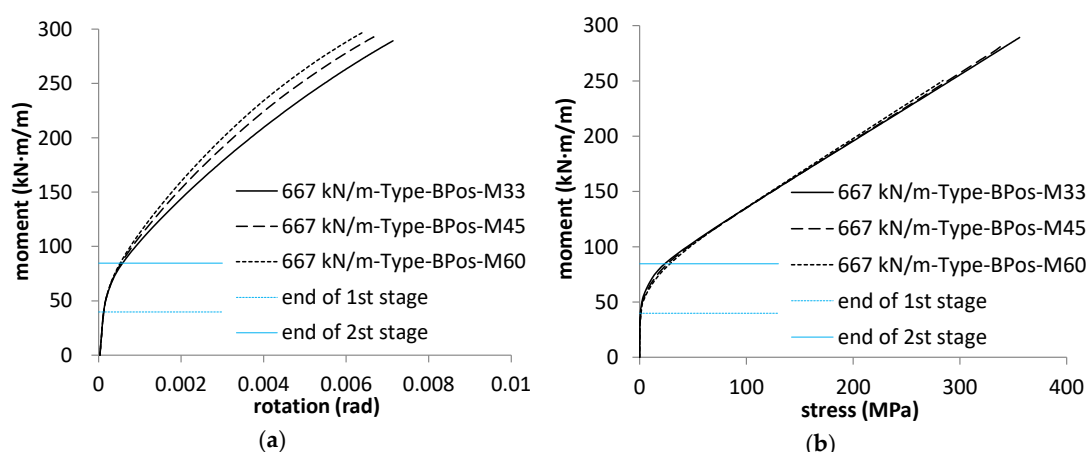


Figure 23. Evolution of the rotations and bolt stresses with different Young's moduli: (a) rotation curves; (b) bolt stress curves.

Table 8. Summary of the rotational stiffnesses during the third stage with different moduli of the bolts (stiffness unit: kN·m/m/rad, modulus unit: GPa).

Modulus	Rotational Stiffness in Positive Cases		Rotational Stiffness in Negative Cases	
	Type-BPos	Increase Rate	Type-BNeg	Increase Rate
200	37,404	-	32,598	-
372	43,187	15%	38,369	18%
661	45,882	23%	42,492	30%

5.3. Influence of Concrete Strength

The effect of concrete strength can be investigated by modifying the concrete strength class. In addition to the design concrete strength class of the segments, C50, the classes C70 and C90 were also investigated. The joint rotation curves and bolt stress curves are shown in Figure 24, and only the results for positive cases under the constant 667 kN/m axial force are presented for brevity. There are only slight rotation differences at the first stage, and the differences are gradually noticeable at the second and the third stages.

However, the observed bolt stress curves for C70 and C90 are identical to that of C50. These observations show that there is little difference between the bolt elongations in these cases, and that some differences in the rotation curves occur for the different concrete classes. The classes C70 and C90 have higher Young's moduli and result in smaller deformations of the compression zone. The average rotational stiffness during the third stage for different concrete classes is summarized in Table 9. Compared to the average stiffness at the third stage for the C50 class, the stiffnesses for C70 and C90 increase by 3% and 6%, respectively. The corresponding stiffness increases in the negative cases are 9% and 15%. Within the bending moment range under normal service conditions, the effect of adopting higher concrete classes on the joint deformation is very limited.

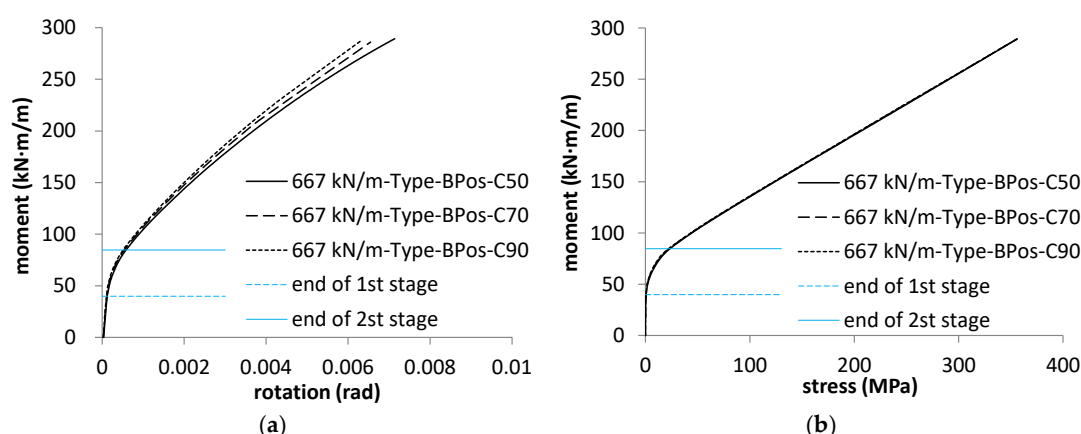


Figure 24. Evolution of the rotations and bolt stresses with different concrete classes: (a) rotation curves; (b) bolt stress curves.

Table 9. Summary of the rotational stiffnesses during the third stage with different concrete classes (stiffness unit: kN·m/m/rad, modulus unit: GPa).

Concrete Class	Rotational Stiffness in Positive Cases		Rotational Stiffness in Negative Cases	
	Type-BPos	Increase Rate	Type-BNeg	Increase Rate
C50	37,404	-	32,598	-
C70	38,431	3%	35,406	9%
C90	39,602	6%	37,342	15%

Although an increase of the concrete strength class, the bolt diameter, and the number of bolts have a positive influence on the joint rotation, the effect of bolt repositioning is more efficient. It is found that adapting the joint section to increase the lever arm between the bolts and the compression zone is the most efficient optimizing method. It also increases the joint's bearing capacity for bending moments, as discussed in Section 4. The increase of the bolt diameters or the number of bolts is a relatively effective way to improve the joint rotational behavior under normal service conditions when compared to adopting higher concrete classes.

6. Conclusions

In this paper, for the joints equipped with DIJP components, joint tests and FEM joint simulations were both conducted to investigate the joint behavior before and after the bolt position improvements. The joint model provides an efficient approach for exploring the influence of the internal forces in the joint's vicinity and the effect of other optimizing methods, such as concrete strength class, bolt diameters, and the number of bolts. From the analysis of the joints with DIJPs, the following conclusions can be drawn:

1. The failure of the joints is initiated by concrete cracking at the core section and is terminated by concrete crushing. At that stage, the bolts do not yield, and thus provide an additional safety margin. This type of joint failure mode is similar to that of a column cross-section with small eccentricity. For the joints under positive bending moments, the joint stiffness increases once the outer edges of the segments touch each other.
2. The joint's resistance to cracking and the ultimate bearing capacity after bolt position improvements are both enhanced. The resistance to cracking increases by 33.6% for positive cases and by 18.0% for negative cases. The resistance to crack penetration increases by 13.8% for positive cases and 18.4% for negative cases.
3. The connecting reinforcements between DIJPs and concrete can guarantee the DIJPs' anchorage in the concrete. The components of the DIJPs and their connections in this new joint type are proven to be reliable.
4. For a given axial force, the joint behavior can be divided into three stages. At the first stage, the whole joint core section is under compression, and bolts do not contribute to the rotation resistance. The joint behavior is governed by the structural details of the core section. At the second stage, the bolts start being tensioned. The bolt stress increases fairly quickly while the rotational stiffness decreases gradually. At the third stage, the lever arm exceeds the distance from the edge of the outer section to the joint central axis. The evolutions of the joint rotation and the bolt stress appear to be almost linear.
5. When compared to an increase of the concrete strength class, an increase of the bolt diameter, or an increase in the number of bolts, a change of the joint section to increase the lever arm between the bolts and the compression zone can most effectively improve the joint behavior, resulting in a decrease of the bolt stresses, as well as an increase of the joint rotation stiffness and of the joint bearing capacity. This optimization direction should be preferably considered when designing a joint section.

Author Contributions: Conceptualization, methodology, writing—original draft preparation, W.Z.; formal analysis, validation, software, W.Z. and W.D.C.; writing—review and editing, supervision, W.D.C. and L.T.; project administration, funding acquisition, X.L. All authors have read and agreed to the published version of the manuscript.

Funding: This research was funded by the National Natural Science Foundation of China (grant number 51578409) and the China Scholarship Council. The financial support is gratefully acknowledged.

Institutional Review Board Statement: Not applicable.

Informed Consent Statement: Not applicable.

Data Availability Statement: Data is contained within the article.

Acknowledgments: The authors express their gratitude to Ningbo Rail Transit Group Co. Ltd. for the cooperation and support in the research.

Conflicts of Interest: The authors declare no conflict of interest.

References

1. Do, N.-A.; Dias, D.; Oreste, P.; Djeran-Maigre, I. Three-dimensional numerical simulation of a mechanized twin tunnels in soft ground. *Tunn. Undergr. Space Technol.* **2014**, *42*, 40–51. [\[CrossRef\]](#)
2. Lee, K.; Ge, X. The equivalence of a jointed shield-driven tunnel lining to a continuous ring structure. *Can. Geotech. J.* **2001**, *38*, 461–483. [\[CrossRef\]](#)
3. Li, Z.; Soga, K.; Wang, F.; Wright, P.; Tsuno, K. Behaviour of cast-iron tunnel segmental joint from the 3D FE analyses and development of a new bolt-spring model. *Tunn. Undergr. Space Technol.* **2014**, *41*, 176–192. [\[CrossRef\]](#)
4. Do, N.-A.; Dias, D.; Oreste, P. Three-dimensional numerical simulation of mechanized twin stacked tunnels in soft ground. *J. Zhejiang Univ. Sci. A* **2014**, *15*, 896–913. [\[CrossRef\]](#)
5. Blom, C. Design Philosophy of Concrete Linings for Tunnels in Soft Soils. Ph.D. Thesis, Delft University of Technology, Delft, The Netherlands, 2002.

6. Lee, K.; Hou, X.; Ge, X.; Tang, Y. An analytical solution for a jointed shield-driven tunnel lining. *Int. J. Numer. Anal. Methods Geomech.* **2001**, *25*, 365–390. [\[CrossRef\]](#)
7. Working Group NO.2., International Tunnelling Association. Guidelines for the design of shield tunnel lining. *Tunn. Undergr. Space Technol.* **2000**, *15*, 303–331. [\[CrossRef\]](#)
8. Liu, X.; Sun, Q. Case analysis on progressive collapse of shield tunnel linings. *J. Tunn. Hazard Control* **2020**, *2*, 21–30.
9. Yu, H.; Yuan, Y.; Qiao, Z.; Gu, Y.; Yang, Z.; Li, X. Seismic analysis of a long tunnel based on multi-scale method. *Eng. Struct.* **2013**, *49*, 572–587. [\[CrossRef\]](#)
10. Li, X.; Yan, Z.; Wang, Z.; Zhu, H. Experimental and analytical study on longitudinal joint opening of concrete segmental lining. *Tunn. Undergr. Space Technol.* **2015**, *46*, 52–63. [\[CrossRef\]](#)
11. Liu, X.; Bai, Y.; Yuan, Y.; Mang, H.A. Experimental investigation of the ultimate bearing capacity of continuously jointed segmental tunnel linings. *Struct. Infrastruct. Eng.* **2016**, *12*, 1364–1379. [\[CrossRef\]](#)
12. Li, X.; Yan, Z.; Wang, Z.; Zhu, H. A progressive model to simulate the full mechanical behavior of concrete segmental lining longitudinal joints. *Eng. Struct.* **2015**, *93*, 97–113. [\[CrossRef\]](#)
13. Liu, X.; Dong, Z.; Bai, Y.; Zhu, Y. Investigation of the structural effect induced by stagger joints in segmental tunnel linings: First results from full-scale ring tests. *Tunn. Undergr. Space Technol.* **2017**, *66*, 1–18. [\[CrossRef\]](#)
14. Liu, X.; Zhang, C.; Zhang, C.; Yuan, Y. Ultimate load-carrying capacity of the longitudinal joints in segmental tunnel linings. *Concr. Constr.* **2017**, *18*, 693–709. [\[CrossRef\]](#)
15. Koyama, Y. Present status and technology of shield tunneling method in Japan. *Tunn. Undergr. Space Technol.* **2003**, *18*, 145–159. [\[CrossRef\]](#)
16. Jin, Y.; Ding, W.; Yan, Z.; Soga, K.; Li, Z. Experimental investigation of the nonlinear behavior of segmental joints in a water-conveyance tunnel. *Tunn. Undergr. Space Technol.* **2017**, *68*, 153–166. [\[CrossRef\]](#)
17. Yan, Z.; Peng, Y.; Ding, W.; Zhu, H.; Huang, F. Load tests on segment joints of single lining structure of shield tunnel in Qingcaosha water conveyance project. *Chin. J. Geotech. Eng.* **2011**, *33*, 1385–1390.
18. Zhou, L.; Zhu, H.-H.; Yan, Z.-G.; Shen, Y.; Meng, H.; Guan, L.-X.; Wen, Z.-Y. Experimental testing on ductile-iron joint panels for high-stiffness segmental joints of deep-buried drainage shield tunnels. *Tunn. Undergr. Space Technol.* **2019**, *87*, 145–159. [\[CrossRef\]](#)
19. Cao, Y.; Wang, P.; Jin, X.; Wang, J.; Yang, Y. Tunnel structure analysis using the multi-scale modeling method. *Tunn. Undergr. Space Technol.* **2012**, *28*, 124–134. [\[CrossRef\]](#)
20. Yu, H.; Yuan, Y.; Chen, Z.; Yu, G. Numerical simulation for large-scale seismic response analysis of long-distance water-conveyance shield tunnel. In Proceedings of the ICPTT 2009: Advances and Experiences with Pipelines and Trenchless Technology for Water, Sewer, Gas, and Oil Applications, Shanghai, China, 18–21 October 2009; American Society of Civil Engineers: Reston, VA, USA, 2009; pp. 1197–1211.
21. Zhang, W.; Wang, J.; Jin, M.; Koizumi, A. Numerical analysis of DRC segment under inner water pressure based on full-scale test verification for shield tunnel. *Tunn. Undergr. Space Technol.* **2016**, *56*, 157–167. [\[CrossRef\]](#)
22. Zhu, Y.; Zhu, Y.; Huang, D.; Li, P. Development and application of the technical system for quasi-rectangular shield tunnelling. *Mod. Tunn. Technol.* **2016**, *53*, 1–12. [\[CrossRef\]](#)
23. Liu, X.; Liu, Z.; Yuan, Y.; Zhu, Y. Quasi-Rectangular Shield Tunneling Technology in the Ningbo Rail Transit Project. In Proceedings of the High Tech Concrete: Where Technology and Engineering Meet, Maastricht, The Netherlands, 12–14 June 2017; Springer International Publishing: Cham, Switzerland, 2017; pp. 2765–2773. [\[CrossRef\]](#)
24. Chow, B. Double-O-tube shield tunneling technology in the Shanghai Rail Transit Project. *Tunn. Undergr. Space Technol.* **2006**, *21*, 594–601. [\[CrossRef\]](#)
25. Ye, G.; Hashimoto, T.; Shen, S.; Zhu, H.; Bai, T. Lessons learnt from unusual ground settlement during Double-O-Tube tunnelling in soft ground. *Tunn. Undergr. Space Technol.* **2015**, *49*, 79–91. [\[CrossRef\]](#)
26. Nakamura, H.; Kubota, T.; Furukawa, M.; Nakao, T. Unified construction of running track tunnel and crossover tunnel for subway by rectangular shape double track cross-section shield machine. *Tunn. Undergr. Space Technol.* **2003**, *18*, 253–262. [\[CrossRef\]](#)
27. Ding, W.; Gong, Y.; Qiao, Y.; Gong, C. Experimental investigation on mechanical behavior of segmental joint under combined loading of compression-bending-shear. *Tunn. Undergr. Space Technol.* **2020**, *98*, 103346. [\[CrossRef\]](#)
28. Zhang, H.; Fu, D.; Guo, C. Study on load test of segment joint in shield driven tunnel. *Mod. Tunn. Technol.* **2002**, *39*, 28D34.
29. Abaqus. *Abaqus (2018) User's Manual*; Abaqus Inc.: Johnston, RI, USA, 2018.
30. Liu, X.; Liu, Z.; Ye, Y.; Bai, Y.; Zhu, Y. Mechanical behavior of quasi-rectangular segmental tunnel linings: Further insights from full-scale ring tests. *Tunn. Undergr. Space Technol.* **2018**, *79*, 304–318. [\[CrossRef\]](#)
31. Liu, X.; Ye, Y.; Liu, Z.; Huang, D. Mechanical behavior of Quasi-rectangular segmental tunnel linings: First results from full-scale ring tests. *Tunn. Undergr. Space Technol.* **2018**, *71*, 440–453. [\[CrossRef\]](#)
32. Zhang, W.; De Corte, W.; Liu, X.; Taerwe, L. Influence of Rotational Stiffness Modeling on the Joint Behavior of Quasi-Rectangular Shield Tunnel Linings. *Appl. Sci.* **2020**, *10*, 8396. [\[CrossRef\]](#)